Check for updates

ADVANCED SUSTAINABLE SYSTEMS
www.advsustainsys.com

Surface Defect Engineered Nano-Cu/TiO_2 Photocatalysts for Hydrogen Production

Letizia Liccardo, Paolo Moras, Polina M. Sheverdyaeva, Alberto Vomiero, Alfonso Caballero, Gerardo Colón, and Elisa Moretti**

Surface defects engineered nano-Cu/TiO_2 photocatalysts are synthesized through an easy and cost-effective microwave-assisted hydrothermal synthesis, mixing commercial P25 titania (TiO_2) and oxalic acid (Ox), followed by 2.0 wt% Cu co-catalyst (labeled as $Cu_{2.0}$) loading through in situ photodeposition during reaction. The hydrothermal treatment does not affect the catalyst crystalline structure, morphology, nor the surface area. However, depending on the Ox/TiO_2 molar ratio used an influence on the optical properties and on the reactivity of the system is detected. The presence of surface defects leads to intraband states formation between valence band and conduction band of bare titania, inducing an important enhancement in the photoactivity. Thus, $Cu_{2.0}$/gOx/P25 200 (where g is the weight of Ox and 200 the temperature in Celsius degrees used during the synthesis) have been successfully tested as efficient photocatalysts for hydrogen production through methanol (MeOH) reforming under UV light in a MeOH/ H_2O solution (10% v/v) by fluxing the system with N_2, showing an increased reactivity compared to the bare $Cu_{2.0}$/P25 system.

1. Introduction

The global energy crisis caused by the latest events is having far-reaching implications and natural gas is center stage. The average cost of electricity is greatly increasing and high prices for both fossil fuels and natural gas are the main cause.[1] In a possible scenario, energy demand will rise dramatically, thus people may not be able to afford modern electricity, reverting to the use of traditional biomass and by soaring greenhouse gas emissions into atmosphere. Oil and coal are only a poor and short-term option, and the crisis may be seen as a boost for low-emission alternatives.[2]

As a result, the clean-energy economy is emerging and hydrogen, thanks to its potential as a clean and energy vector, is considered an ideal candidate, playing a crucial role within this transition process. Furthermore, hydrogen can be produced from a variety of processes and feedstocks, including renewable resources such as biomass or water by using renewable energy sources such as solar light.[3] Sunlight is the most abundant renewable source, and it can provide energy to our earth, which is significantly larger than the daily total global energy consumption. Researchers have been focused on H_2 production through solar water splitting methods.[4] However, the efficiency values for their practical use are still too low.[5] In this frame, H_2 production from alcohol photocatalytic reforming reaction is one of the most suitable alternatives in the field of heterogenous photocatalysis.[5] In general, well-designed semiconductor photocatalysts with tailored properties are needed. The main drawbacks that hamper the development at a large-scale concern indeed the catalyst performance. As a matter of fact, back-reactions, the fast photogenerated charge-carriers recombination or the deactivation of the catalyst due to poor stability, are the main issues to overcome their practical exploitation.[6,7]

Thanks to its unique properties and versatility, titania has always been considered an ideal candidate for photocatalytic application such as H_2 production from alcohol photo reforming. However, its wide bandgap (3.0–3.2 eV) that hinders the use of full solar light spectrum, combined with all the aforementioned deficiencies are limiting its practical use.[3,8] Furthermore, large specific surface area, high crystallinity and anatase phase are known to increase photocatalytic activity. Intense investigations

L. Liccardo, A. Vomiero, E. Moretti
Department of Molecular Sciences and Nanosystems
Ca' Foscari University of Venice
Via Torino 155, Venezia Mestre 30172, Italy
E-mail: elisam@unive.it

P. Moras, P. M. Sheverdyaeva
Istituto di Struttura della Materia-CNR (ISM-CNR)
SS 14, Km 163.5, Trieste 34149, Italy

A. Vomiero
Division of Materials Science
Department of Engineering Sciences and Mathematics
Luleå University of Technology
Luleå 97187, Sweden

A. Caballero, G. Colón
Instituto de Ciencia de Materiales de Sevilla
Centro Mixto Universidad de Sevilla-CSIC
Américo Vespucio 49, Sevilla 41092, Spain
E-mail: gcolon@icmse.csic.es

The ORCID identification number(s) for the author(s) of this article can be found under https://doi.org/10.1002/adsu.202300418

© 2023 The Authors. Advanced Sustainable Systems published by Wiley-VCH GmbH. This is an open access article under the terms of the Creative Commons Attribution-NonCommercial-NoDerivs License, which permits use and distribution in any medium, provided the original work is properly cited, the use is non-commercial and no modifications or adaptations are made.

DOI: 10.1002/adsu.202300418

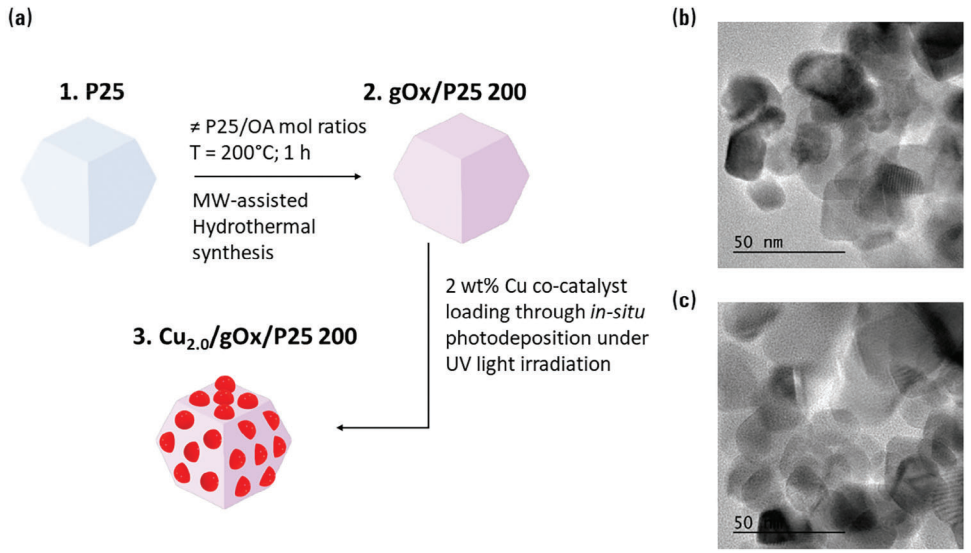

Figure 1. a) Synthesis scheme. TEM images of b) bare P25 and c) 2.5Ox/P25 200.

are still ongoing on different aspects of photocatalytic activity of TiO_2, which can be exploited to improve its performances, including doping and co-doping,[9] nanostructuring,[10] defect engineering,[11,12] reactor configuration,[13] heterostructuring,[14] among the others.

According to the reported literature, among several types of photocatalysts, commercial titania P25 from Evonik is often taken as target material since it shows excellent performance.[3] In fact, P25 is composed of a phase combination ratio between anatase and rutile and an average crystallite size of ≈20 nm, having all the features required to show good photoactivity, that can be further enhanced.[15,16] In general, a good strategy to increase TiO_2 efficiency is the tuning of its optical and electronic properties, by metal co-catalyst loading and simultaneously working on chemical surface composition.[8,15,17]

It is well known that the use of a metal co-catalyst can hinder the fast charge-carriers recombination but, in addition to this traditional strategy, surface defects engineering has been suggested as a novel approach to improve the overall photocatalytic efficiency. In fact, surface defects can induce modifications on the charge distribution around Ti and O, enhancing the separation of the photocarriers, promoting the sacrificial agent adsorption, and extending the light absorption range.[18]

In the present work, surface defect engineered nano-Cu/TiO_2 ($Cu_{2.0}$/gOx/P25 200) photocatalysts have been synthesized through an easy and cost-effective microwave (mw)-assisted hydrothermal synthesis, mixing commercial P25 and oxalic acid (Ox), followed by nominal 2.0 wt% metal co-catalyst (Cu) loading through chemical reduction deposition procedure (see **Figure 1a**). In detail, it is possible to obtain surface defects engineered commercial P25 nanoparticles combined with the use of Cu co-catalyst to improve the electron-hole separation and broaden the absorbance ability, thanks to the presence of mid-gap states below the TiO_2 conduction band, and the photocatalytic activity, thanks to high surface-to-volume ratio, stability of the crystalline structure and finally, enhancement of charge-carriers separation.

2. Results and Discussion

Surface defects engineered nano-TiO_2 photocatalysts were synthesized through an easy mw-assisted hydrothermal synthesis, mixing commercial P25 titania and Ox in different molar ratios (Ox/P25). Samples were labeled as gOx/P25 200, where *g* is the weight of oxalic acid and 200 the temperature (in Celsius degrees) used during the synthesis (Figure 1a step 1 and 2). Subsequently, nominal 2 wt% of Cu (labeled as $Cu_{2.0}$) co-catalyst was loaded through an in situ photodeposition when the photocatalytic tests under UV light irradiation (using a 365 nm UV LED array equipped in the photoreactor) were performed (Figure 1a step 3). In this first section, we report and deeply investigate gOx/P25200 samples, to better understand how the mw-treatment in combination with the oxalic acid can induce surface modifications.

2.1. Morphological and Structural Characterization

The crystal structure of the prepared materials was characterized by X-ray diffraction (XRD) and micro-Raman analysis. **Figure 2** shows the XRD patterns for gOx/P25200 samples, compared with commercial P25, taken as a reference, and the JCPDS cards 21–1276 (rutile) and 21–172 (anatase). As it can be noticed, all the gOx/P25200 samples displayed the typical pattern of commercial P25, including both rutile and anatase phases, which is more evident from the intense peaks located at 2θ 25.3°, 37.7°, 48.0°, 53.9°, and 55.02° corresponding to the (101), (004), (200), (105), and (211) reflections. The addition of oxalic acid during the hydrothermal treatment at 200 °C does not affect the overall crystal structure of commercial P25 which remains stable, as confirmed also by Raman analysis. In fact, as widely reported in literature, the six main Raman active modes for anatase TiO_2 (A_{1g} + $2B_{1g}$ + 3Eg symmetries) are commonly detected at 143, 196, 398, 519 (superimposed with 515 cm^{-1} band), 639 cm^{-1}, corresponding to E_g, E_g, B_{1g}, A_{1g}, B_{1g}, and E_g vibrational modes.[15,19] Moreover, as expected, rutile TiO_2 Raman active modes can only be foreseen

© 2023 The Authors. Advanced Sustainable Systems published by Wiley-VCH GmbH

23667486, 2024, 3, Downloaded from https://onlinelibrary.wiley.com/doi/10.1002/adsu.202300418 by Alberto Vomiero - Cochraneltalia , Wiley Online Library on [25/07/2024]. See the Terms and Conditions (https://onlinelibrary.wiley.com/terms-and-conditions) on Wiley Online Library for rules of use; OA articles are governed by the applicable Creative Commons License

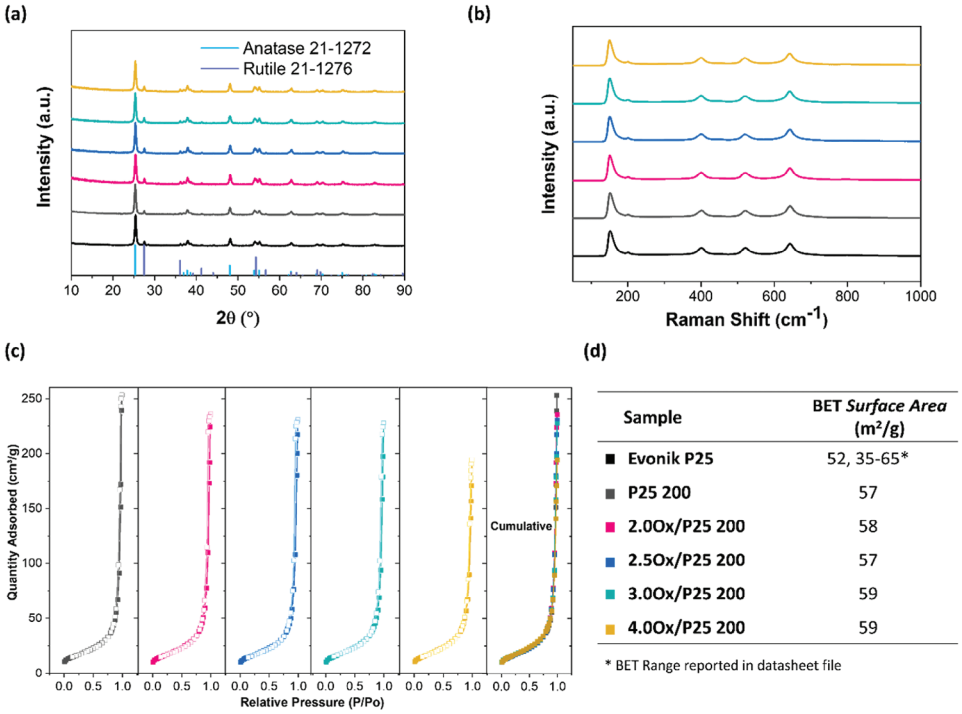

Figure 2. a) XRD patterns; b) Raman spectra; c) N_2 adsorption-desorption isotherms for P25 200 and gOx/P25 200 samples; d) BET surface area values for all the samples including the Evonik P25 reference. All the curves in (a–c) follow the color palette reported in (d).

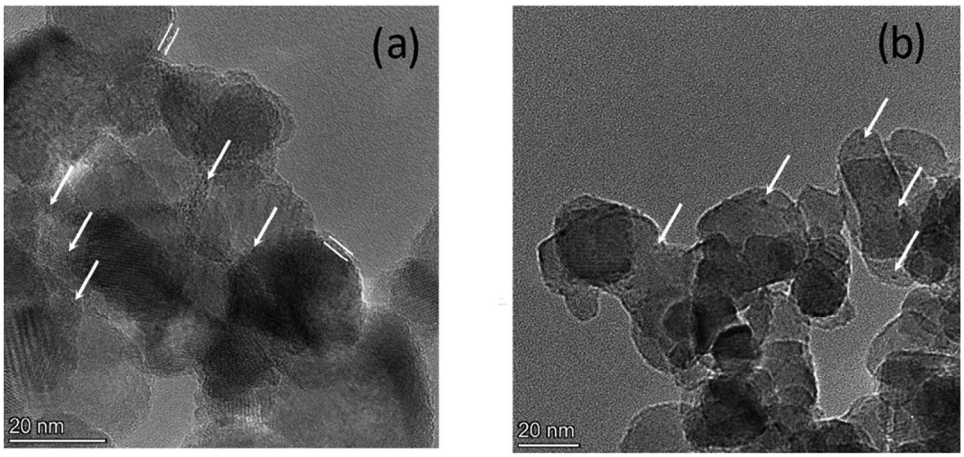

Figure 3. HRTEM images for a) $Cu_{2.0}$/3.0Ox/P25 200 and b) $Cu_{2.0}$/P25 200. In both the panels, the white arrows indicate Cu clusters.

at 140 (B_{1g}), 235 (multiphoton process), 445 (E_g), 609 (A_{1g}), and 825 cm^{-1} (B_{2g}) (Figure 2b).[20] gOx/P25200 samples showed the typical P25 Raman peaks, confirming no apparent changes in the crystal structure. From TEM micrographs (Figure 1b,c) and BET analysis (Figure 2c,d), we can observe that neither the shape nor the morphology and the textural properties of commercial P25 are influenced by the addition of Ox and subsequent hydrothermal treatment, suggesting only the presence of surface modifications. As evidenced in the table of Figure 2d, no relevant differences on the surface areas calculated from the N_2 adsorption-desorption isotherms are detected. In fact, Evonik P25 shows a measured surface area of 52 $m^2 \cdot g^{-1}$ in the range between 35 and 65 $m^2 \cdot g^{-1}$ (values reported in the data sheet file, as expected), which is similar to that of 4Ox/P25 sample (59 $m^2 \cdot g^{-1}$), treated with the highest amount of Ox during the mw-assisted synthesis.

In **Figure 3** we show the HRTEM images for $Cu_{2.0}$/P25 200 and $Cu_{2.0}$/3.0Ox/P25 200 catalysts. The first important issue we can highlight refers to the surface rugosity observed for oxalic acid treated sample (Figure 3a). It is evident that hydrothermal acid treatment leads to the formation of a well-defined amorphous shell of about 2–3 nm. This shell indicates the loss of crystallinity at surface level. Indeed, it is possible to see that anatase planes are

© 2023 The Authors. Advanced Sustainable Systems published by Wiley-VCH GmbH

23667486, 2024, 3, Downloaded from https://onlinelibrary.wiley.com/doi/10.1002/adsu.202300418 by Alberto Vomiero - Cochraneltalia , Wiley Online Library on [25/07/2024]. See the Terms and Conditions (https://onlinelibrary.wiley.com/terms-and-conditions) on Wiley Online Library for rules of use; OA articles are governed by the applicable Creative Commons License

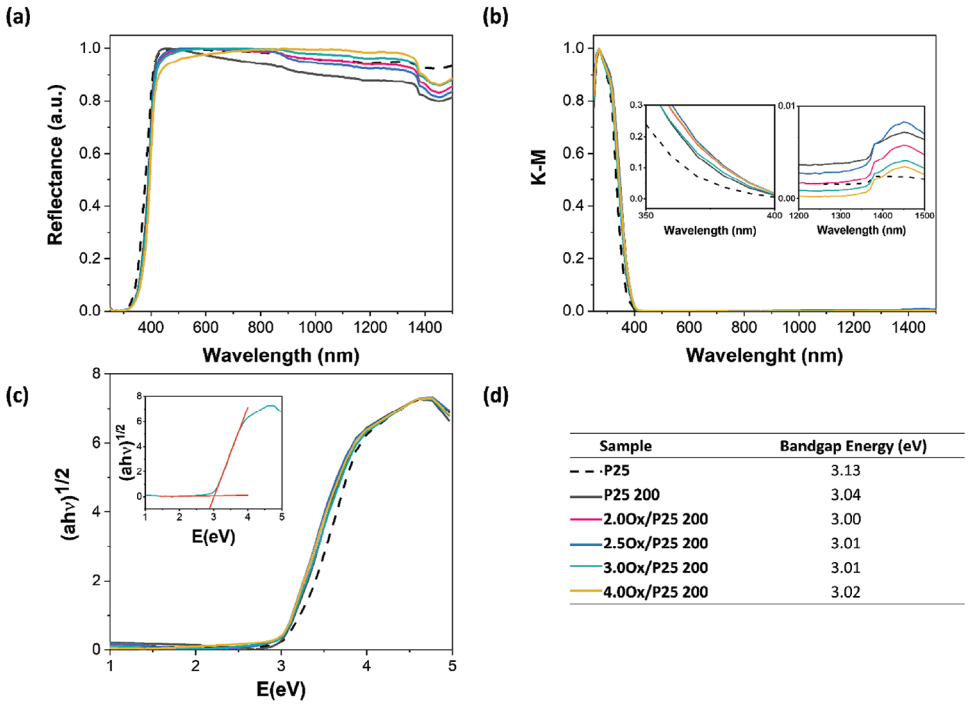

Sample	Bandgap Energy (eV)
P25	3.13
P25 200	3.04
2.0Ox/P25 200	3.00
2.5Ox/P25 200	3.01
3.0Ox/P25 200	3.01
4.0Ox/P25 200	3.02

Figure 4. a) DRUV-vis-NIR spectra; b) Kubelka–Munk functions with inset-graphs focusing on the band changes in UV and NIR region; c) Tauc plots and d) Bandgap energies comparison for all the samples, including Evonik P25 reference.

lost at the surface. This fact is not observed for TiO_2 hydrothermally treated with water, for which particles show flat borders (Figure 3b). Secondly, it is possible to see the effectiveness of copper photodeposition over both TiO_2 support (white arrows in the two panels of Figure 3). However, Cu clusters are more difficult to distinguish on $Cu_{2.0}$/3.0Ox/P25 200 since the cluster size is much smaller (1–2 nm vs 5–6 nm for $Cu_{2.0}$/3.0Ox/P25 200 and $Cu_{2.0}$/P25 200, respectively).

2.2. Optical Properties

All the diffuse reflectance UV–visible–near-infrared (DRUV-vis-NIR) spectra in **Figure** 4a are characterized by the main absorption feature related to the typical optical bandgap of the titania (≈3.1 eV), which induces a strong absorption edge ≈370 nm and is associated to the O^{2-} (2p) → Ti^{4+} (3d) transition. As previously reported, the structure and the morphology of gOx/P25 200 samples are not influenced by the addition of Ox, suggesting only the presence of surface modifications. In the DRUV-vis-NIR analysis, a very small but evident red-shift of the main band toward higher wavelength compared to the bare P25 reference has been detected. The introduction of Ox in combination with the hydrothermal treatment at 200 °C enables an increasing absorbance ability in the region between 350 and 400 nm compared to the bare P25 reference (Figure 4b). This may be ascribed to the presence of surface defects such as Ti^{3+} sites or oxygen vacancies, which result in the introduction of a continuous energy band directly below the conduction band (CB) edge of TiO_2.[18] This is also confirmed by a slight lowering of the bandgap energy values (≈0.1 eV), calculated through the Tauc plot by using the intercept method (Figure 4c,d).[21] Light absorption in the vis–NIR region can be improved by the presence of disordered surface layer or surface defects (i.e., oxygen vacancies).[22–24] Thus, NIR region has also been investigated (Figure 4a,b). Evident changes in all spectra compared to bare P25 can be detected. A wide band centered at 1450 nm and an increase in absorbance capacity from 850 nm occurred for some samples. The onset of the absorption feature at 1450 nm can be attributed to adsorption of water molecules onto the surface of the treated samples P25 200 and gOx/P25 200 with respect to the reference sample P25. In this case, both Ox and the treatment temperature seem to induce some surface modifications by changing the composition of functional groups exposed on the photocatalysts surface. In addition, a higher water adsorption may be ascribed to higher surface content of oxygen vacancies which tend to bind water.[8] This is also confirmed by XPS analysis (see section below).

Since emission processes in semiconductors are strictly related to photogenerated charge carriers recombination,[25] photoluminescence (PL) emission spectra for all gOX/P25 200 samples (including P25 reference) were collected in the range 380–600 nm by using an excitation wavelength of 350 nm (**Figure 5**). One of the most significant drawbacks of TiO_2 is its fast charge carriers recombination. The higher the recombination of free carriers, the higher the PL intensity and, as expected, the highest emission intensity was recorded for bare P25 (dashed black line in Figure 4). It is worth recalling that non-radiative recombination pathways may also occur lowering the overall PL intensity. However, considering similar non-radiative recombination channels for all the samples, the presence of surface defects or adsorbed water molecules seems to decrease the radiative recombination rate resulting in lower emission intensities for all the

© 2023 The Authors. Advanced Sustainable Systems published by Wiley-VCH GmbH

23667486, 2024, 3, Downloaded from https://onlinelibrary.wiley.com/doi/10.1002/adsu.202300418 by Alberto Vomiero - Cochraneltalia , Wiley Online Library on [25/07/2024]. See the Terms and Conditions (https://onlinelibrary.wiley.com/terms-and-conditions) on Wiley Online Library for rules of use; OA articles are governed by the applicable Creative Commons License

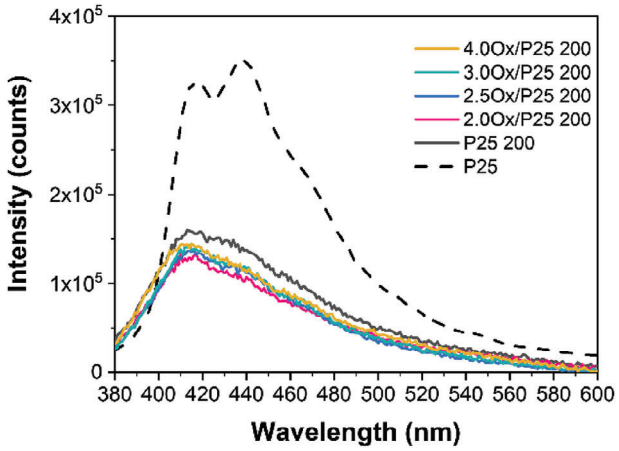

Figure 5. Photoluminescence spectra for all gOX/P25 200 samples, including Evonik P25 reference.

treated samples. Surface defects such as oxygen vacancies or Ti^{3+} act as trapping centers for the photo-excited electrons,[26] providing active sites for the electron transfer processes. Furthermore, the presence of OH groups or water molecules onto the metal oxide surface promotes the trapping phenomena by decreasing electron-hole pairs radiative recombination as well.[27] Consequently, the overall charge-carriers separation efficiency of the photocatalyst is enhanced.

2.3. XPS Analysis

Core level XPS data were acquired for the P25, P25 200 and gOx/P25 200 samples at $h\nu = 750$ eV (**Figure 6**). The O1s spectra were fitted with four components. From the low to the high binding energy side these components correspond to O^{2-} of stoichiometric TiO_2 (530.20 –530.40 eV), OH groups adsorbed on TiO_2 (531.60 –532.20 eV), O (532.65 –532.95 eV), and OH (534.05 –534.3 eV) groups bound to C,[28] which is a surface contaminant. The last component is also associated with the presence of H_2O [29] and displays the most notable increase along the sequence of spectra. This trend could be the fingerprint of an increasing density of surface oxygen vacancies, which tend to bind efficiently H_2O. The Ti2p spectra could be fitted with one doublet attributed to Ti^{4+}, while there is no evidence of defective Ti^{3+}. The O/Ti atomic ratio for the different materials can be derived from the area of the O^{2-} peak and the Ti^{4+} doublet normalized to the respective photoemission cross sections at $h\nu = 750$ eV (0.24 and 0.7[30]). It is evaluated to be 2.09 ± 0.09 for all samples, i.e., very close to the expected ratio 2. **Table 1** reports the Ti/O atomic ratios for all the samples. Moreover, as amount of oxalic acid increased the deconvoluted contributions at energies above 531 eV increases, denoting a higher hydroxylation of the surface leading to a progressively higher O/Ti.

The valence band spectra acquired at $h\nu = 468$ eV do not display sizable differences in the O2p-derived states (4 –9 eV binding energy). Within the gap region (zoom), O vacancy-related feature at 1.25 eV is observed to increase in intensity along the sequence of the P25, P25 200 and 2.0Ox/P25 200 samples. For the other three samples this feature broadens significantly and gives rise

Table 1. O/Ti ratio in the P25, P25 200 and gOx/P25 200 samples.

Sample	O/Ti ratio
P25	2.10
P25 200	2.05
2.0Ox/P25 200	2.02
2.5Ox/P25 200	2.12
3.0Ox/P25 200	2.17
4.0Ox/P25 200	2.12

to two peaks centered at 1.45 and 0.30 eV. This behavior can be associated with surface modifications induced by the treatments with oxalic acid, which give rise to the shell observed in Figure 3a. Although the present dataset does not allow to describe the microscopic origin of the new in-gap states, we observe that their location is compatible with defect states close to the bottom of the conduction band of TiO_2.

The XPS data were also acquired for the $Cu_{2.0}$/P25 and $Cu_{2.0}$/3.0Ox/P25 200 samples (**Figure 7**). In both cases, the binding energy of the Cu3p peaks ($Cu3p_{3/2}$ at 75.40 eV) and the absence of correlation features on the high binding energy side, which characterize CuO,[31] indicate the formation of Cu_2O on the surface of the Cu co-catalyst.[32] The O1s spectra differ from the corresponding O1s spectra before the addition of Cu (Figure 6) mainly in the relative weight of the peak at 530.40 eV, which derives from the overlapping O^{2-} components of TiO_2 and Cu_2O. The Ti2p spectra are very similar to those observed in Figure 6. The broad valence band feature at ≈4.00 eV is ascribed to the Cu3d states of the Cu_2O surface oxide. The photoemission signal from Cu4sp states, which overlaps to the bandgap region of the P25 and 3.0Ox/P25 200 substrates, does not allow to identify the presence of defect states in the proximity of the Fermi level.

2.4. Photocatalytic H_2 Production

The photocatalytic activity of gOx/P25200 samples was evaluated for the H_2 production through methanol reforming under UV light, at room temperature and P_{atm} by using a continuous flow reactor (Apria Systems). The H_2 production rates and the yield evolution over time referred to methanol photoreforming reaction are reported in **Figure 8**. Furthermore, in Figure 8d the band scheme for electron-hole separation of $Cu_{2.0}$/gOx/P25 200 catalysts has been proposed according to literature[26,27,33] and our deep investigation. As already mentioned, the nominal loading of 2.0 wt% (see Experimental Section for further details) of Cu as co-catalyst has been obtained through the in situ photoreduction at the beginning of the photocatalytic test. Thus, copper nanoparticles (Cu NPs) were formed after exciton creation by means of UV light irradiation, giving rise to oxidation and reduction reactions. During the photocatalytic reaction, it is expected that surface defects would play a crucial role. Thus, we may infer that they could act as trapping states for electrons enhancing the separation of photogenerated charge carriers and consequently, the reduction reactions rates, useful not only for the formation of Cu NPs on the surface of gOx/P25 200 catalysts, but also for the H_2 production. Hence, the first step occurring during the photocat-

© 2023 The Authors. Advanced Sustainable Systems published by Wiley-VCH GmbH

23667486, 2024, 3, Downloaded from https://onlinelibrary.wiley.com/doi/10.1002/adsu.202300418 by Alberto Vomiero - Cochraneltalia , Wiley Online Library on [25/07/2024]. See the Terms and Conditions (https://onlinelibrary.wiley.com/terms-and-conditions) on Wiley Online Library for rules of use; OA articles are governed by the applicable Creative Commons License

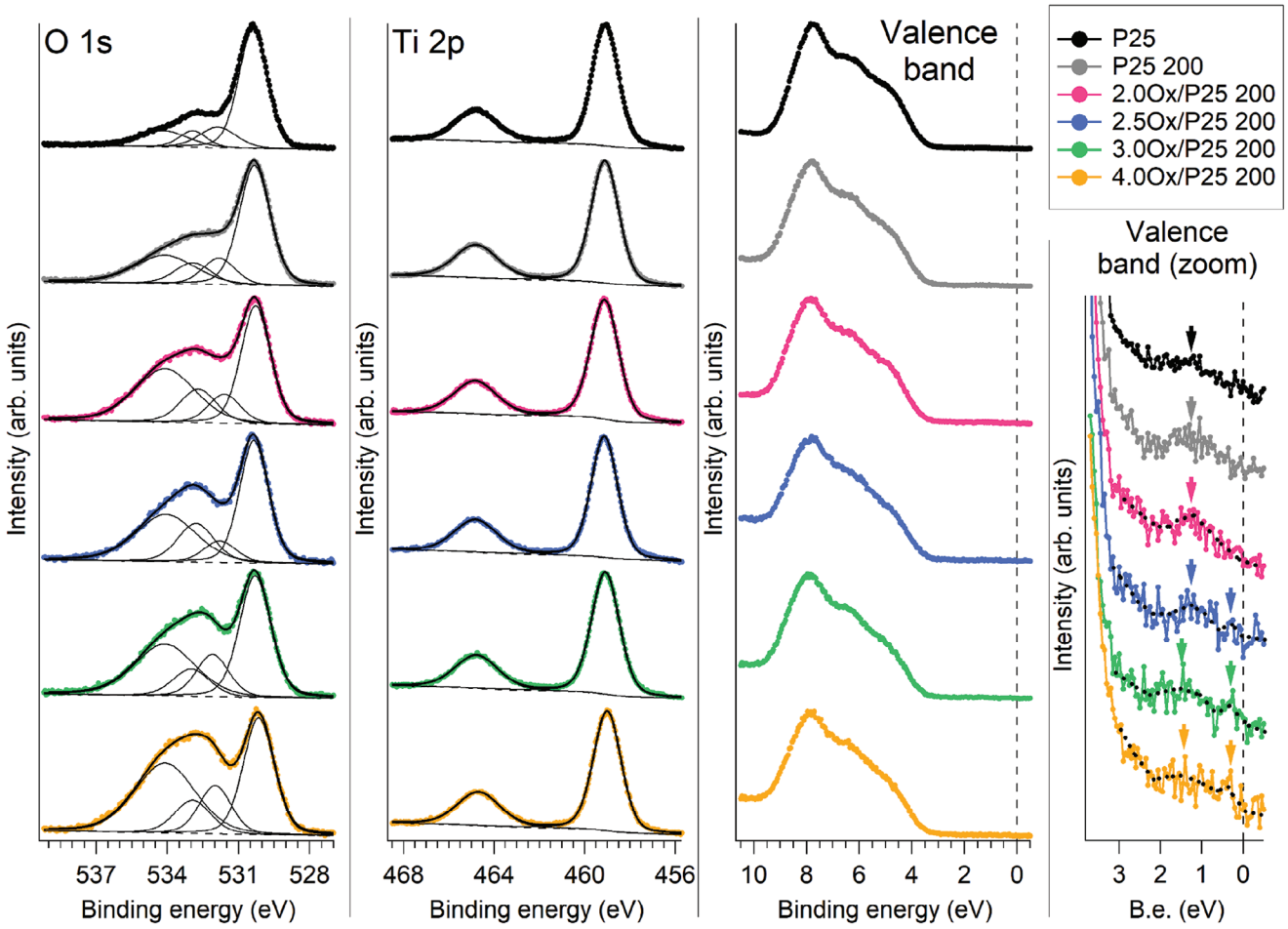

Figure 6. O1s, Ti2p and valence band spectra of the P25, P25 200 and gOx/P25 200 samples. The zoomed valence band spectra indicate the presence of defect states (arrows) in the gap of all samples. Dotted lines are guides to the eye for the identification of the defect-related peaks.

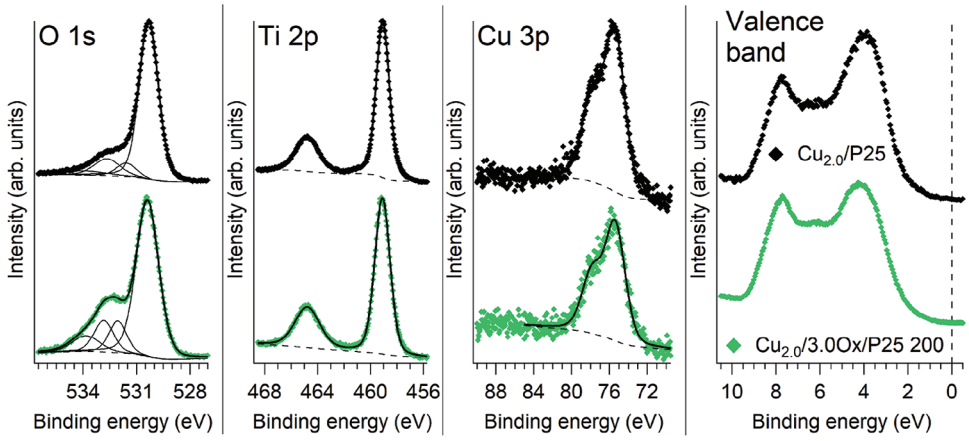

Figure 7. O1s, Ti2p, Cu3p ($h\nu = 750$ eV) and valence band ($h\nu = 469$ eV) spectra of the $Cu_{2.0}$/P25 (*top*) and $Cu_{2.0}$/3.0Ox/P25 200 (*bottom*) samples.

alytic H_2 production is the Cu NPs deposition, also confirmed by a 15-min delay on the H_2 production (see H_2 production rate curves in Figure 8a). The mw-treatment leads to a significant increase in photoreactivity when the loading of Ox during the synthesis is >2.0 g and <4.0 g. In fact, after 6 h of light irradiation, the optimized $Cu_{2.0}$/3Ox/P25200 sample exhibited outstanding photocatalytic H_2 production rates of 6.8 mmol·h^{-1}·g^{-1}, which is two times higher than that of pristine $Cu_{2.0}$/P25 system. Moreover, long-time reaction time for this catalyst shows a rather stable behavior (**Figure 9**). When the Ox loading is below 2.5 g or >3.0 g the

© 2023 The Authors. Advanced Sustainable Systems published by Wiley-VCH GmbH

23667486, 2024, 3, Downloaded from https://onlinelibrary.wiley.com/doi/10.1002/adsu.202300418 by Alberto Vomiero - Cochraneltalia , Wiley Online Library on [25/07/2024]. See the Terms and Conditions (https://onlinelibrary.wiley.com/terms-and-conditions) on Wiley Online Library for rules of use; OA articles are governed by the applicable Creative Commons License

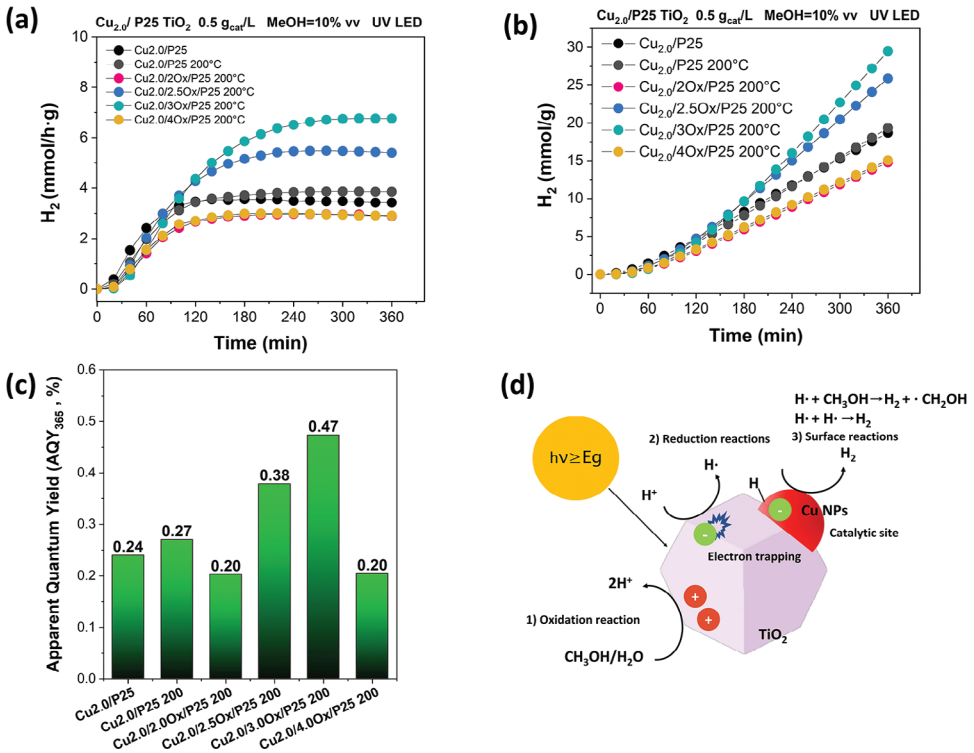

Figure 8. a) H_2 production rates; b) H_2 rates; c) calculated AQYs for $Cu_{2.0}$/P25 $Cu_{2.0}$/P25 200 and $Cu_{2.0}$/gOx/P25 200 photocatalysts; d) Scheme diagram of $Cu_{2.0}$/gOx/P25 200 system.

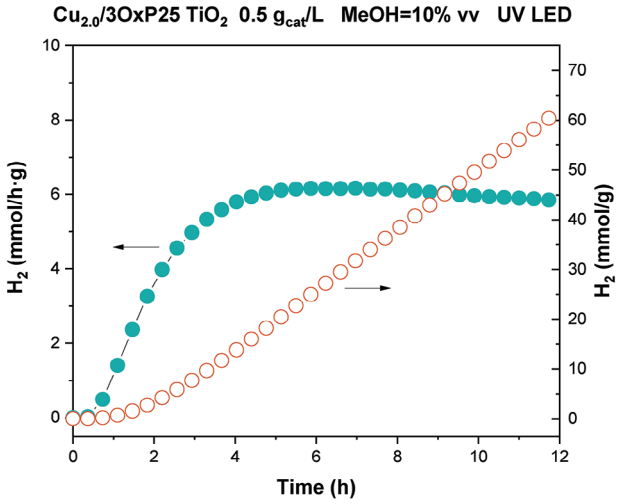

Figure 9. H_2 production rate and yield for $Cu_{2.0}$/3Ox/P25 200 photocatalysts system.

efficiency of the system decreases. This behavior is also marked by the H_2 yields at 6 h of experiment expressed in mmol•g^{-1} and the calculated AQY (Figure 8b,c). $Cu_{2.0}$/3Ox/P25200 is the best performing sample reaching an H_2 yield and an AQY of 29.5 mmol•g^{-1} and 0.47%, respectively, far exceeding $Cu_{2.0}$/P25. Furthermore, after 6 h of experiment the H_2 production reaction reached a steady-state (see the dwell in Figure 8a). Hence, the absence of deactivation during this studied reaction time pointed out the stability of catalyst surface defects.

It is worth mentioning that there are several studies in literature regarding the use of alcohol photoreforming to produce H_2 and each of them is reporting different conditions to optimize the production with their own catalyst/co-catalyst system. For instance, irradiation source, solution composition (water/alcohol ratio) and carrier gas flow are crucial parameters to tune H_2 production rates.[6,7] However, we tried to select some TiO_2/co-catalyst systems to provide a comparison with our samples to highlight their performances by choosing examples tested under similar conditions. Thus, a comparative table is reported (**Table 2**) listing the synthetic method used, the H_2 production rates and apparent quantum yield (AQY) of selected systems concerning the use of TiO_2 in combination with several co-catalysts for the H_2 production through methanol reforming.

As can be observed, the performances of our photocatalytic system are good compared to the listed examples. Furthermore, there is a good compromise between the obtained H_2 production rates, and the synthetic method used in this work. In fact, mw-assisted hydrothermal method followed by the in situ photodeposition can be an innovative way to design a novel and efficient photocatalyst for a future large-scale production.

3. Conclusion

In this work, we have reported an innovative synthesis to obtain a highly active photocatalyst based on the use of surface-defects engineering of TiO_2 in combination with Cu co-catalyst

© 2023 The Authors. Advanced Sustainable Systems published by Wiley-VCH GmbH

23667486, 2024, 3, Downloaded from https://onlinelibrary.wiley.com/doi/10.1002/adsu.202300418 by Alberto Vomiero - Cochraneltalia , Wiley Online Library on [25/07/2024]. See the Terms and Conditions (https://onlinelibrary.wiley.com/terms-and-conditions) on Wiley Online Library for rules of use; OA articles are governed by the applicable Creative Commons License

Table 2. H_2 production rates and apparent quantum yield (AQY) for various TiO_2/co-catalyst systems, tested under similar conditions used in this work (methanol photoreforming reaction under UV light).

System	Co-cat.	Synthetic method	Solution	Irradiation Source	H_2 [mmol g^{-1}•h^{-1}]	AQY [%]	Ref.
1 wt% Pt/TiO_2	Pt	Hydrothermal synthesis in alkaline conditions followed by calcination at 500 °C	25 mL of a 6.7 vol% aqueous methanol solution	LED (λ = 365 nm, 0.438 μmol·s^{-1} of irradiance)	3.6[a)]	∽0.46	[34]
1 wt% NiO/TiO_2	NiO	sol–gel process combined with surfactant-assisted template followed by calcination at 500 °C	200 mL of a 10 vol% aqueous methanol solution	UV 300 W Mercury Lamp	0.8	-	[35]
1.5 wt% NiO/ Anatase TiO_2	NiO	sol–gel process combined with surfactant-assisted template followed by calcination at 500 °C	200 mL of a 10 vol% aqueous methanol solution	UV 300 W Mercury Lamp	0.6	-	[35]
0.4 wt% Au/P25	Au	6 h photodeposition under UV light	75 mL of a 25 vol% aqueous methanol solution	Solarium Philips HB175 lamp (365 nm)	0.4	4.14	[36]
1.5 wt% Au/rutile TiO_2	Au	Hydrothermal synthesis followed by deposition-precipitation with urea method	10 vol% aqueous methanol solution	Spectroline model SB-100P/F lamp (100 W, 365 nm)	0.9	-	[37]
0.5 wt% Au/P25	Au	deposition-precipitation with urea method	200 mL of aqueous methanol solution (1:1 molar ratio)	UV-PC Mercury lamp (2.2 mW·cm^{-2}, 254 nm)	1.9	-	[38]
3 wt% Ru/ TiO_2	Ru	Micro-emulsion method followed by deposition via sonication	50 mL of a 3/7 v/v methanol solution	500 W Xe lamp equipped with a cut-off filter (UV: 280–400 nm)	4.6	-	[39]
1 wt% Nd/ Anatase-brookite TiO_2	Nd	sol–gel method followed by pressurized hot fluids	100 mL of ≈50 vol% aqueous methanol solution	UV 8 W Mercury Lamp (365 nm)	0.7[a)]	-	[40]
6 wt% Bi_2S_3/TiO_2	Bi_2S_3	Sol–gel combined with solvothermal method	200 mL of aqueous methanol solution (1:1 mol ratio)	Mercury Lamp (2.2 mW cm^{-2}, 254 nm)	2.5[a)]	-	[41]
5 wt% Ga_2O_3/TiO_2	Ga_2O_3	Sol–gel and hydrolysis method	200 mL of aqueous methanol (50/50 v/v) solution	Mercury lamp (2.2 mW·cm^{-2}, 254 nm)	0.25[a)]	-	[42]
1 wt% CuO/F- TiO_2	CuO	Sol–gel method followed by impregnation	200 mL of aqueous methanol solution (1:1 v/v)	Mercury lamp (4.4 mW·cm^{-2}, 254 nm)	1.83[a)]	-	[43]
$Cu_{2.0}$/3Ox/P25 200 (optimum)		mw-hydrothermal treatment followed by in situ photodeposition	200 mL of a 10 vol% aqueous methanol solution	365 nm UV LED array	6.8	0.47	This work

[a)] Approximated values from published experimental data.

© 2023 The Authors. Advanced Sustainable Systems published by Wiley-VCH GmbH

23667486, 2024, 3, Downloaded from https://onlinelibrary.wiley.com/doi/10.1002/adsu.202300418 by Alberto Vomiero - Cochraneltalia , Wiley Online Library on [25/07/2024]. See the Terms and Conditions (https://onlinelibrary.wiley.com/terms-and-conditions) on Wiley Online Library for rules of use; OA articles are governed by the applicable Creative Commons License

loaded through in situ photodeposition method. The obtained $Cu_{2.0}$/gOx/P25 200 photocatalysts have shown significant improvement in the photocatalytic H_2 production through methanol reforming reaction with the best-performing sample ($Cu_{2.0}$/3Ox/P25 200) exhibiting outstanding photocatalytic H_2 production rates under UV irradiation of 6.8 mmol·h^{-1}·g^{-1}, two times higher than that of pristine $Cu_{2.0}$/P25 system, as confirmed also by the calculated AQY. Thanks to the use of XPS and optical characterizations, we stated that such a marked increase in the performances of this system is related both to the presence of surface defects, in detail oxygen vacancies, and the use of Cu co-catalyst. In fact, surface defects engineered commercial P25 nanoparticles combined with Cu co-catalyst enable to improve electron-hole separation, broaden the absorbance ability, thanks to the presence of mid-gap states below the TiO_2 conduction band and consequently, increase the overall photocatalytic activity. In conclusion, tailoring the surface properties of commercial P25 might be a good strategy to overcome the fast charge carriers recombination limit of TiO_2 -based photocatalyst leading way for the development of new technologies in the field of energy applications at a large scale.

4. Experimental Section

Materials: The following commercial reagents, without any further purification, were used in all the experimental phases: deionized water (H_2O); commercial TiO_2 (Evonik AEROXIDE TiO_2 P25); oxalic acid (Ox, $H_2C_2O_4$, Sigma–Aldrich 99.0%); copper (II)-nitrate trihydrate ($Cu(NO_3)_2{\cdot}3H_2O$, Merck ≥ 99.0%); methanol (MeOH, Merck ≥ 99.5%).

Photocatalyst Preparation: Surface defects P25 photocatalysts were synthesized by microwave-assisted hydrothermal reaction, mixing commercial P25 and oxalic acid. In a typical synthesis procedure, an aqueous dispersion of P25 was prepared under magnetic stirring. Oxalic acid was added with fixed mole ratios (n/n) between Ox and P25 of 3.7, 4.5, 5.4, and 7.2, respectively. After 30 min stirring, the dispersion was transferred into a 100 mL Teflon-lined microwave reactor and heated at 200 °C and 600 W for 1 h. After cooling to room temperature, the precipitate was separated from the reaction mixture by filtration and washed several times with distilled water. Finally, the obtained specimen was dried in oven at 80 °C overnight. Samples were labeled as gOx/P25200 where *g* refers to the grams of oxalic acid and 200 to the temperature used (i.e., 2Ox/P25 200). To better understand the role of oxalic acid, and the influence of the temperature on bare P25, the same procedure without the addition of Ox was followed, thus obtaining sample for comparison labeled as P25 200. The co-catalyst was loaded on gOx/P25200 surface samples through in situ photoreduction during the first step of the photocatalytic reaction. By this procedure, Cu was well dispersed over the TiO_2 surface showing a particle size of ca. 2–4 nm.[44] In detail, 2 wt% of Cu^{2+} with respect to the catalyst (using a solution of $Cu(NO_3)_2{\cdot}3H_2O$ 0.01 M) was directly added to the MeOH/H_2O solution used for the photocatalytic H_2 production under UV irradiation. Samples were labeled as $Cu_{2.0}$/gOx/P25 200. The deposited Cu loading was determined through the use of a Microwave Plasma-Atomic Emission Spectrometer (Agilent MP-AES 4210) for $Cu_{2.0}$/P25, $Cu_{2.0}$/P25 200, and $Cu_{2.0}$/3Ox/P25 200. Data were acquired after five readings and the mean value was 1.8 wt% for all the samples.

Characterization Techniques: The transmission electron microscopy (TEM) images were obtained by using a FEI S/TEM Talos F200S in the HRTEM mode. The samples were directly dropped on a gold grid.

X-ray diffraction (XRD) patterns were obtained using a Siemens D-501 diffractometer with a Ni filter and a graphite monochromator. The X-ray source was Cu Kα radiation.

For sample identification, diffraction patterns were matched to the JCPDS database.

Micro-Raman spectra were collected using a LabRAM Jobin Yvon spectrometer equipped with a microscope. Laser radiation (λ = 532 nm) was used as an excitation source at 5 mW. All measurements were recorded under the same conditions (2 s of integration time and 30 accumulations) using a 100× magnification objective and a 125 mm pinhole.

Brauner–Emmett–Teller (BET) surface area studies were carried out by N_2 physisorption at −196 °C using a Micromeritics 2000 instrument.

UV–vis–NIR diffuse reflectance (DRUV–vis–NIR) spectra were collected with a Perkin Elmer Lambda 1050+ UV–vis–NIR spectrophotometer, equipped with an integrating sphere, for wavelengths ranging from 200 to 1200 nm. The bandgap (E_g) was determined using the Kubelka–Munk approach (Equation (1)).[21]

$$F(R_\infty) = \frac{(1-R_\infty)^2}{2R_\infty} = \frac{K}{S} \quad (1)$$

Here, $F(R_\infty)$ is the Kubelka–Munk function, R_∞ is the diffuse reflectance, K is the absorption coefficient, and S is the scattering coefficient. Then by exploiting the Tauc method,[45] the bandgap for TiO_2 semiconductors can be expressed using the following equation Equation (2):

$$(F(R_\infty)\,h\nu)^{\frac{1}{2}} = B\left(h\nu - E_g\right) \quad (2)$$

Here, h is the Planck's constant, ν is the frequency of the light and B is a constant. By plotting $F(R_\infty)$ versus the energy expressed in eV, and by finding the *x*-axis intersection point of the linear fit of the Tauc plot, it is possible to estimate the bandgap of a material.

Photoluminescence (PL) measurements were performed in air at room temperature using a FluoroLog 3–21 system (Horiba Jobin-Yvon) equipped with a 450 W xenon arc lamp as excitation source, whose wavelength was selected by a double Czerny–Turner monochromator and signal detection stage including an iHR300 single grating monochromator coupled to a Hamamatsu photomultiplier tube (model R928P for visible range; model R5509-73 N_2-cooled for NIR range). Excitation wavelength was set at 350 nm and PL spectra recorded over a range of 380–600 nm. The XPS measurements were carried out at the VUV-Photoemission beamline of the synchrotron Elettra (Trieste, Italy) using photons of 750 and 469 eV for the core level and valence band analysis, respectively. The spectra were acquired at room temperature with a Scienta R4000 electron spectrometer.

Photocatalytic H_2 Production Tests: The photocatalytic activity of the samples was evaluated for the H_2 evolution reaction from methanol photoreforming. Photocatalytic H_2 production tests were carried out in a liquid-phase flow reactor system supplied by Apria Systems. The photocatalyst was suspended in a MeOH/ H_2O solution (10% v/v) by fluxing the system with N_2(g) at 50 mL·min^{-1} for 60 min before starting the reaction. To start the test, the gas flow was adjusted to 6 mL·min^{-1} and the lamp (365 nm UV LED array) switched on. Such low gas flow (6 mL·min^{-1}) was set just to reach very exigent conditions that allow us to see any small differences between the studied catalyst. A gas chromatographer equipped with a thermal conductivity detector (Agilent 7890B GC) was used to analyze the effluent gases and quantify the H_2 production. Equation (3) was used to estimate the apparent quantum yield (AQY) for the H_2 evolution reaction:[46]

$$AQY = \frac{2 \cdot n_{H_2}}{n_p}\left[\frac{mol \cdot s^{-1}}{mol \cdot s^{-1}}\right] \cdot 100 \quad (3)$$

where n_{H2} is the H_2 molecules number and n_p is the number of incident photons reaching the photocatalyst. n_p was calculated from the ratio between the total incident energy and the energy of one photon. In the experimental setup, the total incident energy was calculated considering the 365 nm incident light used and the power density of the incident light (2100 W·m^{-2}).

© 2023 The Authors. Advanced Sustainable Systems published by Wiley-VCH GmbH

23667486, 2024, 3, Downloaded from https://onlinelibrary.wiley.com/doi/10.1002/adsu.202300418 by Alberto Vomiero - Cochraneltalia , Wiley Online Library on [25/07/2024]. See the Terms and Conditions (https://onlinelibrary.wiley.com/terms-and-conditions) on Wiley Online Library for rules of use; OA articles are governed by the applicable Creative Commons License

Acknowledgements

Elettra Sincrotrone Trieste was acknowledged for providing access to its synchrotron radiation facilities and for financial support under the SUI international project. G.C. acknowledges the financial support from the EU FEDER and Junta de Andalucía under I+D+i Project P20-00156 and the Ministerio de Ciencia e Innovación/FEDER through PLEC202-007906 and TED2021-130173B-C43 projects. Finally, The authors acknowledge Prof. Enrico Trave from Ca'Foscari University of Venice for his support during PL measurements. A.V. acknowledges the Kempe Foundations, the Knut och Alice Wallenberg Foundation, and the European Union – NextGenerationEU – through MUR (National Recovery and Resilience Plan (NRRP) – Mission 4 Component 2, Investment N. ECS00000043 – CUP N. H43C22000540006 (iNEST) and Mission 4 Component 2 Investment 1.3 – CUP D43C22003090001 (NEST)). P.M. and P.M.S. acknowledge EUROFEL-ROADMAP ESFRI of the Italian Ministry of University and Research.

Conflict of Interest

The authors declare no conflict of interest.

Data Availability Statement

The data that support the findings of this study are available from the corresponding author upon reasonable request.

Keywords

H_2 production, methanol photoreforming, photocatalysis, surface defects, TiO_2

Received: September 8, 2023
Revised: November 20, 2023
Published online: December 21, 2023

[1] International Energy Agency, International Energy Agency (IEA) World Energy Outlook **2022**, *2022*.
[2] World Meteorological Organization (WMO), WMO Global Annual to Decadal Climate Update, Geneva, **2023**.
[3] A. Kubacka, M. Fernández-García, G. Colón, *Chem. Rev.* **2012**, *112*, 1555.
[4] L. Liccardo, E. Lushaj, L. Dal Compare, E. Moretti, A. Vomiero, *Small Sci.* **2022**, *2*, 2100104.
[5] G. Colón, *Appl. Catal. A Gen.* **2016**, *518*, 48.
[6] M. I. Maldonado, A. López-Martín, G. Colón, J. Peral, J. I. Martínez-Costa, S. Malato, *Appl. Catal. B Environ.* **2018**, *229*, 15.
[7] A. Ruiz-Aguirre, J. G. Villachica-Llamosas, M. I. Polo-López, A. Cabrera-Reina, G. Colón, J. Peral, S. Malato, *Energy* **2022**, *260*, 125199.
[8] L. Liccardo, M. Bordin, P. M. Sheverdyaeva, M. Belli, P. Moras, A. Vomiero, E. Moretti, *Adv. Funct. Mater.* **2023**, *33*, 2370138.
[9] R. Hossain, M. A. Uddin, M. A. Khan, *J. Phys. Chem. C* **2023**, *127*, 10897.
[10] C. J. Querebillo, *Nanomaterials* **2023**, *13*, 982.
[11] L. Liao, M. Wang, Z. Li, X. Wang, W. Zhou, *Nanomaterials* **2023**, *13*, 468.
[12] Y. Zhang, J. Yan, *Chem. Eng. J.* **2023**, *472*, 144831.
[13] R. B. Domínguez-Espíndola, D. M. Arias, C. Rodríguez-González, P. J. Sebastian, *Appl. Therm. Eng.* **2022**, *216*, 119009.
[14] L. Biswal, R. Mohanty, S. Nayak, K. Parida, *J. Environ. Chem. Eng.* **2022**, *10*, 107211.
[15] H. Lu, B. Zhao, R. Pan, J. Yao, J. Qiu, L. Luo, Y. Liu, *RSC Adv.* **2014**, *4*, 1128.
[16] L. Mino, G. Spoto, S. Bordiga, A. Zecchina, *J. Phys. Chem. C* **2012**, *116*, 17008.
[17] K. C. Christoforidis, P. Fornasiero, *ChemCatChem* **2019**, *11*, 368.
[18] G. Colón, M. C. Hidalgo, G. Munuera, I. Ferino, M. G. Cutrufello, J. A. Navío, *Appl. Catal. B Environ.* **2006**, *63*, 45.
[19] S. Wang, L. Yi, J. E. Halpert, X. Lai, Y. Liu, H. Cao, R. Yu, D. Wang, Y. Li, *Small* **2012**, *8*, 265.
[20] M. González-Tejero, J. G. Villachica-Llamosas, A. Ruiz-Aguirre, G. Colón, *ACS Appl. Energy Mater.* **2023**, *6*, 4007.
[21] P. Kubelka, F. Munk, *Z. Tech. Phys.* **1931**, *12*, 593.
[22] Y. Wang, J. Cai, M. Wu, H. Zhang, M. Meng, Y. Tian, T. Ding, J. Gong, Z. Jiang, X. Li, *ACS Appl. Mater. Interfaces* **2016**, *8*, 23006.
[23] T. Xia, Y. Zhang, J. Murowchick, X. Chen, *Catal. Today* **2014**, *225*, 2.
[24] X. Chen, L. Liu, P. Y. Yu, S. S. Mao, *Science* **2011**, *331*, 746.
[25] J. Ma, T. J. Miao, J. Tang, *Chem. Soc. Rev.* **2022**, *51*, 5777.
[26] L. Yan, C. Jing, *J. Phys. Chem. Lett.* **2020**, *11*, 9485.
[27] E. Han, K. Vijayarangamuthu, J.-S. Youn, Y.-K. Park, S.-C. Jung, K.-J. Jeon, *Catal. Today* **2018**, *303*, 305.
[28] B. Gupta, N. Kumar, K. Panda, V. Kanan, S. Joshi, I. Visoly-Fisher, *Scientific Reports* **2017**, *7*, 45030.
[29] I. Luciu, R. Bartali, N. Laidani, *J. Phys. D. Appl. Phys.* **2012**, *45*, 345302.
[30] J. J. Yeh, *Atomic Calculation of Photoionization Cross-Section and Asymmetry Parameters*, Gordon and Breach Science Publishers, Langhorne, PE, USA **1993**.
[31] I. Khalakhan, M. Vorokhta, X. Xie, L. Piliai, I. Matolínová, *J. Electron Spectros. Relat. Phenomena* **2021**, *246*, 147027.
[32] T. Robert, M. Bartel, G. Offergeld, *Surf. Sci.* **1972**, *33*, 123.
[33] F. Platero, A. López-Martín, A. Caballero, G. Colón, *ChemCatChem* **2021**, *13*, 3878.
[34] Y.-H. Chung, K. Han, C.-Y. Lin, D. O'neill, G. Mul, B. Mei, C.-M. Yang, *Catal. Today* **2020**, *356*, 95.
[35] T. Sreethawong, Y. Suzuki, S. Yoshikawa, *Int. J. Hydrogen Energy* **2005**, *30*, 1053.
[36] J. A. Ortega Méndez, C. R. López, E. Pulido Melián, O. González Díaz, J. M. Doña Rodríguez, D. Fernández Hevia, M. Macías, *Appl. Catal. B Environ.* **2014**, *147*, 439.
[37] W.-T. Chen, A. Chan, Z. H. N. Al-Azri, A. G. Dosado, M. A. Nadeem, D. Sun-Waterhouse, H. Idriss, G. I. N. Waterhouse, *J. Catal.* **2015**, *329*, 499.
[38] S. Oros-Ruiz, R. Zanella, R. López, A. Hernández-Gordillo, R. Gómez, *J. Hazard. Mater.* **2013**, *263*, 2.
[39] W. Ouyang, M. J. Muñoz-Batista, A. Kubacka, R. Luque, M. Fernández-García, *Appl. Catal. B Environ.* **2018**, *238*, 434.
[40] K. Kočí, I. Troppová, M. Reli, L. Matějová, M. Edelmannová, H. Drobná, L. Dubnová, A. Rokicińska, P. Kuśtrowski, L. Čapek, *Front. Chem.* **2018**, *6*, 44.
[41] C. García-Mendoza, S. Oros-Ruiz, A. Hernández-Gordillo, R. López, G. Jácome-Acatitla, H. A. Calderón, R. Gómez, *J. Chem. Technol. Biotechnol.* **2016**, *91*, 2198.
[42] M. Navarrete, S. Cipagauta-Díaz, R. Gómez, *J. Chem. Technol. Biotechnol.* **2019**, *94*, 3457.
[43] C. Castañeda, F. Tzompantzi, A. Rodríguez-Rodríguez, M. Sánchez-Dominguez, R. Gómez, *J. Chem. Technol. Biotechnol.* **2018**, *93*, 1113.
[44] F. Platero, A. López-Martín, A. Caballero, T. C. Rojas, M. Nolan, G. Colón, *ACS Appl. Nano Mater.* **2021**, *4*, 3204.
[45] P. Makula, M. Pacia, W. Macyk, *J. Phys. Chem. Lett.* **2018**, *9*, 6814.
[46] M. Qureshi, K. Takanabe, *Chem. Mater.* **2017**, *29*, 158.

© 2023 The Authors. Advanced Sustainable Systems published by Wiley-VCH GmbH

23667486, 2024, 3, Downloaded from https://onlinelibrary.wiley.com/doi/10.1002/adsu.202300418 by Alberto Vomiero - Cochraneltalia , Wiley Online Library on [25/07/2024]. See the Terms and Conditions (https://onlinelibrary.wiley.com/terms-and-conditions) on Wiley Online Library for rules of use; OA articles are governed by the applicable Creative Commons License